

# Hausdorff Distance Matching with Adaptive Query Denoising for Rotated Detection Transformer

Hakjin Lee<sup>\*†</sup> Minki Song<sup>\*</sup> Jamyoun Koo Junghoon Seo  
SI-Analytics

{hakjinlee, minkisong, jmkoo, jhseo}@si-analytics.ai

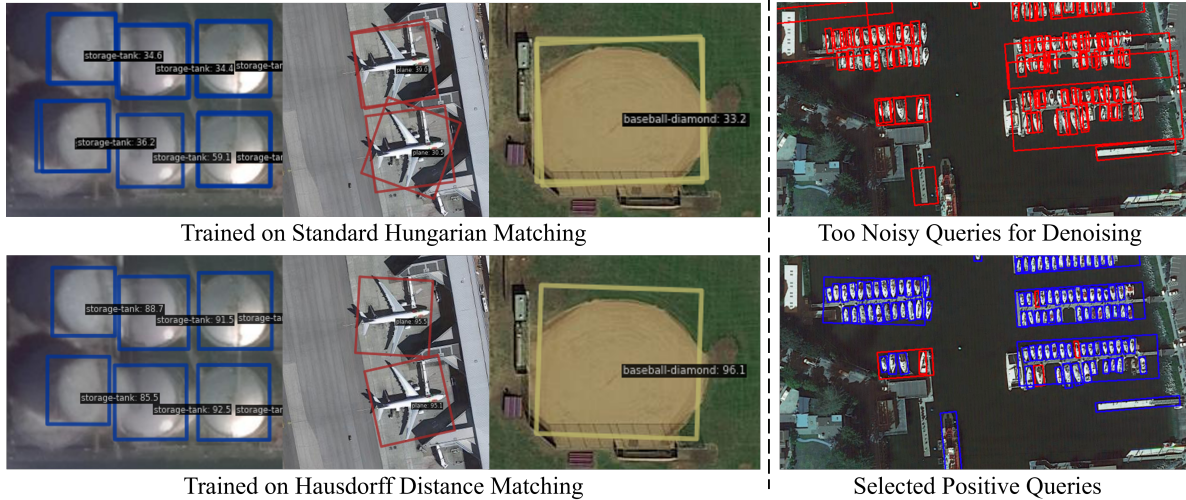


Figure 1. Main contributions of this work. **Left:** The introduced hausdorff distances addresses the duplicate low-confidence predictions from the baseline. **Right:** Proposed adaptive query denoising employs Hungarian matching between **positive noised queries** and **accurate predictions** to selectively filter queries for denoising.

## Abstract

The Detection Transformer (DETR) has emerged as a pivotal role in object detection tasks, setting new performance benchmarks due to its end-to-end design and scalability. Despite its advancements, the application of DETR in detecting rotated objects has demonstrated suboptimal performance relative to established oriented object detectors. Our analysis identifies a key limitation: the L1 cost used in Hungarian Matching leads to duplicate predictions due to the square-like problem in oriented object detection, thereby obstructing the training process of the detector. We introduce a Hausdorff distance-based cost for Hungarian matching, which more accurately quantifies the discrepancy between predictions and ground truths. Moreover, we note that a static denoising approach hampers the training of rotated DETR, particularly when the detector’s pre-

dictions surpass the quality of noised ground truths. We propose an adaptive query denoising technique, employing Hungarian matching to selectively filter out superfluous noised queries that no longer contribute to model improvement. Our proposed modifications to DETR have resulted in superior performance, surpassing previous rotated DETR models and other counterparts. This is evidenced by our model’s state-of-the-art achievements in benchmarks such as DOTA-v1.0/v1.5/v2.0, and DIOR-R.

## 1. Introduction

In the field of aerial and satellite imagery analysis, the use of oriented bounding boxes is essential to accurately detecting densely packed, arbitrary-oriented objects with minimal overlap [15, 47]. A variety of rotated object detectors have been developed by adapting traditional convolution-based object detectors to handle these oriented objects, yielding promising outcomes [13, 18, 19, 26, 40, 41, 48, 49, 51, 53,

<sup>\*</sup>Equal Contribution.

<sup>†</sup>Corresponding author.

55–57, 59, 60]. Typically, this adaptation involves the incorporation of more complex, hand-designed components, such as rotated anchor priors or intricate box representations.

The advent of the Detection Transformer (DETR) has unveiled new possibilities for end-to-end object detection, notably eliminating the need for these complex, hand-designed components [3]. Subsequent advancements have focused on mitigating the slow training convergence of DETR by introducing various methods such as deformable attention [67], formulating queries as learnable anchor boxes [33], and incorporating a query denoising task [33, 62]. Notably, DINO [62] has set new benchmarks in the COCO object detection landscape, demonstrating remarkable scalability [30, 46, 50, 68]. However, the application of DETR in oriented object detection remains an under-explored avenue in recent studies, presenting an opportunity for significant advancements in this field [10, 39, 61, 65].

First, we have observed that an adept implementation and adaptation of DETR for oriented object detection can yield competitive results, rivaling existing oriented object detectors, as shown in Table 1. This observation stands in contrast to prior studies, which have reported only suboptimal performances in the absence of complex new designs, such as feature alignment [2, 10, 13], or unique box representations [17, 61, 65]. Detailed information regarding the development of our rotated DETR baseline, including implementation specifics, is provided in the Appendix 6.

Nonetheless, our observations have identified two critical challenges impeding the stable training of our baseline DETR model, as illustrated in Figure 1. The first challenge involves the occurrence of duplicate low-confidence predictions which contradicts a crucial property of DETRs in preventing such duplications. To address this, we analyzed the impact of L1 distance on Hungarian matching in rotated DETRs. We revealed that it results in spatially inconsistent cost matching between ground truths and predictions. Our solution involves replacing the L1 distance with the Hausdorff distance, which more accurately quantifies these discrepancies. The second challenge arises with the query denoising method, particularly when the model’s predictions become more accurate than the noised ground truths. While initially beneficial in accelerating early-stage DETR training, this method poses challenges in later stages as the distant noised ground truth continues to be recognized as the target, despite the model’s precise predictions. To resolve this, we introduce an adaptive query denoising strategy, employing Hungarian matching to selectively filter out these unhelpful positive noised queries. With these advancements in our model, RHINO, achieves the new state-of-art on DOTA-v1.0/v1.5/v2.0, and DIOR-R benchmarks under single-scale training and testing.

In summary, our research has made the following key

Model	Reported by	Backbone	Epochs	AP <sub>50</sub>	AP <sub>75</sub>
Deformable DETR [67]	Dai et al. [10]	R-50	50	41.86	-
Deformable DETR	Zeng et al. [61]	R-50	50	63.42	26.92
Deformable DETR	Ours	R-50	50	68.50	38.13
Deformable DETR Two-Stage	Ours	R-50	50	70.48	40.07
O <sup>2</sup> -DETR*	Ma et al. [39]	R-50	50	72.15	-
ARS-DETR	Zeng et al. [61]	R-50	36	73.79	49.01
D2Q-DETR*	Zhou et al. [65]	R-50	50	76.58	-
AO <sup>2</sup> -DETR	Dai et al. [10]	R-50	50	77.73	-
DINO [62] (Our baseline)	Ours	R-50	12	76.10	48.20
DINO (Our baseline)	Ours	R-50	36	74.56	49.63

Table 1. Comparison on DOTA-v1.0 between our baseline and past studies on DETRs for oriented object detection. \* indicates multi-scale training and testing

contributions:

- We introduce the Hausdorff distance cost to alleviate the duplicate low-confidence predictions encountered with the use of L1 distance in Hungarian Matching. This method not only addresses the issue of duplicate predictions but also leads to more stable training and enhanced performance.
- We propose an adaptive query denoising method that utilizes Hungarian matching to selectively filter out noised ground truths as the model’s predictions become more accurate, thereby significantly boosting performance in the later stages of training.
- Our proposed model establishes a new state-of-the-art benchmark in performance on the DOTA v1.0/v1.5/v2.0, and DIOR-R datasets.

We hope that our work paves the way for further exploration and advancement of query-based object detectors for oriented object detection.

## 2. Method

### 2.1. Preliminaries

In this section, we provide a concise overview of set prediction and Hungarian matching in the Detection Transformer (DETR). In order to enable set prediction without duplicate predictions, the Detection Transformer employs Hungarian matching loss during its training phase. In the training phase, a Hungarian matching component assigns each prediction result with one ground truth according to the minimum cost between every prediction and ground truth. The model is then trained to minimize the loss from these assigned results, resulting in predicting a single object for one target, in contrast to other detectors which assign multiple predictions to a single ground truth. Here, ‘cost’ metrics for Hungarian matching and ‘loss’ metrics for training a Detection Transformer are commonly aligned to preserve consistency between the training objective and the strategy for assigning predictions to ground truths. Several DETR models, including the original DETR, Deformable DETR, DN-DETR, DAB-DETR, and DINO, adopt a combination



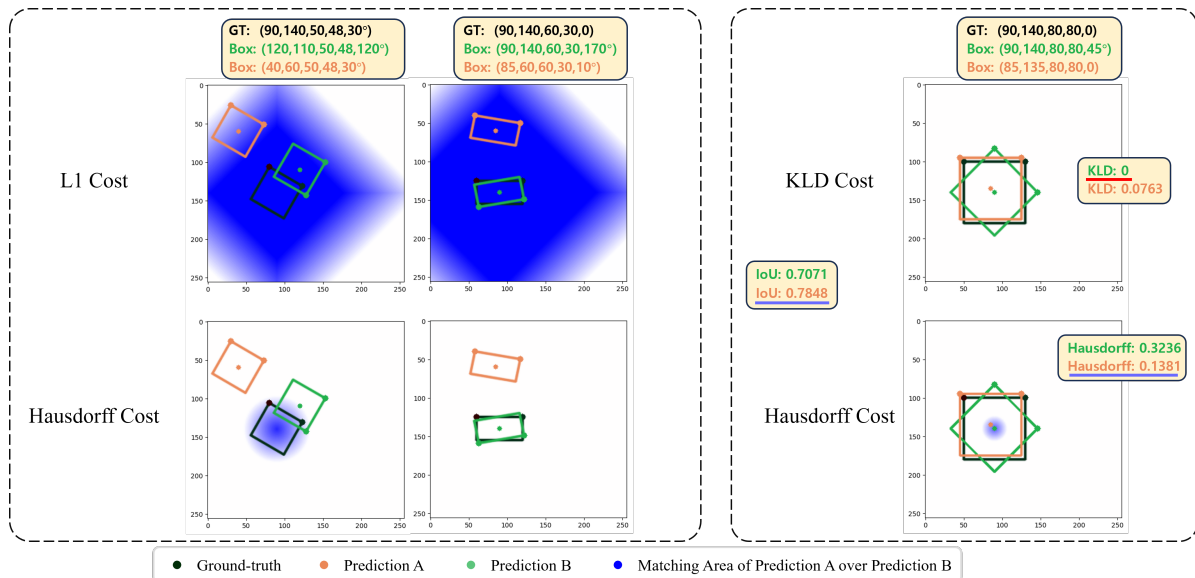


Figure 2. Matching areas of the *Prediction A* to the ground truth. The blue area indicates the orange box is matched to the ground truth over the green box, as the center of the orange box moves along a coordinate axis. In each case, both the ground truth and the green box are fixed. **Left:** Using L1 cost, the orange box which is too far from the ground truth is matched to it over the green box. **Right:** When using the KLD cost, the matching ignores the axis alignment between two boxes. Conversely, the Hausdorff cost takes this into account.

of metrics for both Hungarian matching and the training objective. These metrics include Focal loss [31] for classification, L1 loss, and the Generalized Intersection over Union (GIoU) loss [43] for box regression. The overall metric is mathematically expressed as:

$$\mathcal{L}_{\text{train}} = \lambda_{\text{cls}} \cdot \mathcal{L}_{\text{cls}} + \mathcal{L}_{\text{box}}, \quad (1)$$

$$\mathcal{L}_{\text{box}} = \lambda_{\text{L1}} \cdot \mathcal{L}_{\text{L1}} + \lambda_{\text{IoU}} \cdot \mathcal{L}_{\text{IoU}}, \quad (2)$$

where  $\lambda$  denotes the weight term assigned to each component to control its impact on the training objective.

## 2.2. Building a Strong Baseline for Rotated DETRs

Transitioning from traditional horizontal bounding box detectors to rotated box detectors presents significant challenges. Recent advancements in DETR, such as iterative reference points refinement [67], the use of queries as dynamic anchor boxes [33], and the contrastive query denoising training [62], require meticulous integration into the rotated DETR frameworks to be effective.

Our primary approach to constructing a generalized DETR baseline for oriented object detection involves the natural incorporation of these components. We have expanded the standard 4D coordinates  $\mathbf{b} = \{b_x, b_y, b_w, b_h\}$  of the regression head output to 5D coordinates  $\mathbf{b} = \{b_x, b_y, b_w, b_h, b_{\text{rad}}\}$ , thereby eliminating the need for an additional angle head branch. The angle values, expressed in radians, are mapped from  $[0, \pi)$  to the range of  $[0, 1]$ , similar to other parameters such as center point coordinates,

width, and height. For the IoU term,  $\mathcal{L}_{\text{IoU}}$ , we adopt a KLD loss [56] as the default metric for both the matching cost and IoU loss. In addition, we have adopted other techniques introduced in Deformable DETR (deformable attention, iterative refinement, and two-stage) [67], DAB-DETR (queries as dynamic anchor boxes) [33], DN-DETR (denoising training) [27], and DINO (contrastive denoising training, mixed query selection, and look forward twice) [62]. Further implementation details can be found in Appendix 6.

Table 1 shows the comparison between our implementation and that from the previous works. Our implementation, even without incorporating domain-specific improvements like rotated feature refinement, exhibits competitive performance. This is noticeable when benchmarked against previous DETR models for oriented object detection on the DOTA-v1.0 dataset [47].

## 2.3. Boundary Discontinuity in Hungarian Matching

DETR’s direct set prediction approach via bipartite matching is well-known to enable non-duplicate predictions without requiring postprocessing such as NMS [3]. However, our observations indicate a persistent issue of duplicate predictions under specific conditions, as shown in the left image of Figure 1 and Table 7b. These duplicate predictions frequently occur with lower confidence scores and are particularly noticeable in square-like objects.

The square-like problem, and related boundary discontinuity problem in oriented object detection, have been

demonstrated in previous studies [53, 55]. These studies suggest that the use of common regression loss, such as  $l_n$ -norms, in training oriented object detectors may lead to an unexpected increase in loss due to angle parameterization. In the context of Hungarian matching in DETR, this issue impacts not only the unexpected regression loss peak but also the classification of the model, as the localization cost plays a crucial role in determining the assignment of predictions to ground truths.

Figure 2 presents common scenarios where the unexpected prediction is matched to the ground truth, despite the presence of a more suitable prediction. In our analysis, we investigate whether the ground truth is matched to the *Prediction A* (orange box) or the *Prediction B* (green box), under varying conditions. We compare the matching costs to the ground truth for both the orange box and the green box, where the center of the orange box moves along a coordinate axis. Before computing the cost, box coordinates  $\{b_x, b_y, b_w, b_h, b_{rad}\}$  are normalized with the image sizes and the maximum angle value  $\{I_w, I_h, I_w, I_h, \pi\}$  for the L1 cost. The heatmap intensity is highlighted when the cost of matching the orange box to the ground truth is lower than that of matching the green box to the same ground truth. This indicates that the orange box is preferred for matching the ground truth over the green box when the center of the orange box is within the areas highlighted in blue. As depicted in Figure 2, the L1 cost often favors matching the ground truth with the prediction having the same angle, even in instances where the green box exhibits a higher IoU. This is due to the L1 cost placing excessive emphasis on the angle difference, even after the angle has been normalized. Consequently, this leads to an unstable matching process. Predictions that are too far from a certain ground truth, but sharing the same angle, are more likely to have been predicted for the other targets.

## 2.4. Hausdorff distance for Hungarian Matching

To address the square-like problem and boundary discontinuity caused by the L1 cost, we introduce the Hausdorff distance [1] for Hungarian matching in our model. The Hausdorff distance is mathematically defined as the maximum distance between two sets of points, which can be expressed as follows:

$$d_H(X, Y) = \max \left\{ \sup_{x \in X} d(x, Y), \sup_{y \in Y} d(X, y) \right\}. \quad (3)$$

In the simplest form, we can represent the bounding box by the set of its four corner coordinates. Using this representation, it is possible to calculate the maximum value of pairwise distances between two boxes. In a more general form, we can determine the midpoints of each edge of the bounding box and use these midpoints to calculate the pairwise maximum distance. For the Hausdorff distance, box coordinates

are normalized using the factors  $\{I_w, I_h, I_w, I_h, 1\}$  to preserve the angle values. As shown in Figure 2, using the Hausdorff cost leads to more reasonable matching compared to the L1 cost. Moreover, the Hausdorff distance considers the axis alignment of two boxes, resulting in a more accurate matching compared to 2-D Gaussian distribution-based metrics such as KLD [56], GWD [55].

## 2.5. Adaptive Query Denoising

To further investigate the denoising training strategy [27], we provide a visualization of the positive noised queries and query proposals generated by the model trained for 36 epochs in the right panel of Figure 1. It becomes evident that a significant portion of positive noised queries are not ideally suited for accurate classification. For instance, in the right image of Figure 1, a positive query generated outside the ship should be classified as a ship. In order to filter unhelpful positive noised queries as training progresses, we propose an adaptive query denoising strategy using Hungarian matching. We denote predictions as  $\mathbf{p} = \{p_0, p_1, \dots, p_{N-1}\}$ , where  $N$  is the number of predicted objects, and ground truths as  $\mathbf{y} = \{y_0, y_1, \dots, y_{M-1}\}$  for  $M$  ground truth objects. We refer to noised queries in a denoising group as  $\mathbf{q}^{\text{pos}} = \{q_0^{\text{pos}}, q_1^{\text{pos}}, \dots, q_{M-1}^{\text{pos}}\}$  for positive queries and  $\mathbf{q}^{\text{neg}} = \{q_0^{\text{neg}}, q_1^{\text{neg}}, \dots, q_{M-1}^{\text{neg}}\}$  as negative queries, which are generated from  $M$  ground truths by adding noise. Not to filter out accurately refined queries, we use refined noised queries through decoder layers  $\mathbf{p}^{\text{pos}} = f_{\text{refine}}(\mathbf{q}^{\text{pos}})$  and  $\mathbf{p}^{\text{neg}} = f_{\text{refine}}(\mathbf{q}^{\text{neg}})$  instead of directly using  $\mathbf{q}^{\text{pos}}$  and  $\mathbf{q}^{\text{neg}}$ . Each element  $p_i, y_j, p_k^{\text{pos}}, p_l^{\text{neg}}$  is composed of  $(c, \mathbf{b})$  where  $c$  is the target class and  $\mathbf{b} = \{b_x, b_y, b_w, b_h, b_{rad}\}$  is a 5D rotated box coordinate. The reconstruction loss in a single denoising group can be formulated as follows:

$$\mathcal{L}_{\text{denoising}}(\mathbf{p}^{\text{pos}}, \mathbf{p}^{\text{neg}}, \mathbf{y}) = \sum_{i=0}^{M-1} \mathcal{L}_{\text{pos}}(p_i^{\text{pos}}, y_i) + \mathcal{L}_{\text{neg}}(p_i^{\text{neg}}, \emptyset), \quad (4)$$

where  $\mathcal{L}_{\text{neg}}(p_i^{\text{neg}}, \emptyset)$  indicates a classification loss such as Focal loss for no object  $\emptyset$ .

To remove excessively noisy positive queries,  $\mathcal{L}_{\text{pos}}(p_i^{\text{pos}}, y_i)$  is partitioned into two parts: the base training objective  $\mathcal{L}_{\text{train}}$  and the background loss  $\mathcal{L}_{\text{neg}}$  for filtered queries as below:

$$\mathcal{L}_{\text{pos}}(p_i^{\text{pos}}, y_i) = \mathbb{1}_{\{\hat{\sigma}_i=i\}} \mathcal{L}_{\text{train}}(p_i^{\text{pos}}, y_i) + \mathbb{1}_{\{\hat{\sigma}_i \neq i\}} \mathcal{L}_{\text{neg}}(p_i^{\text{pos}}, \emptyset), \quad (5)$$

where  $\hat{\sigma}_i$  indicates the matching index for a ground truth  $y_i$ . The matching indices are determined by finding the optimal assignment between ground truths and a concatenated list of positive queries and predictions:

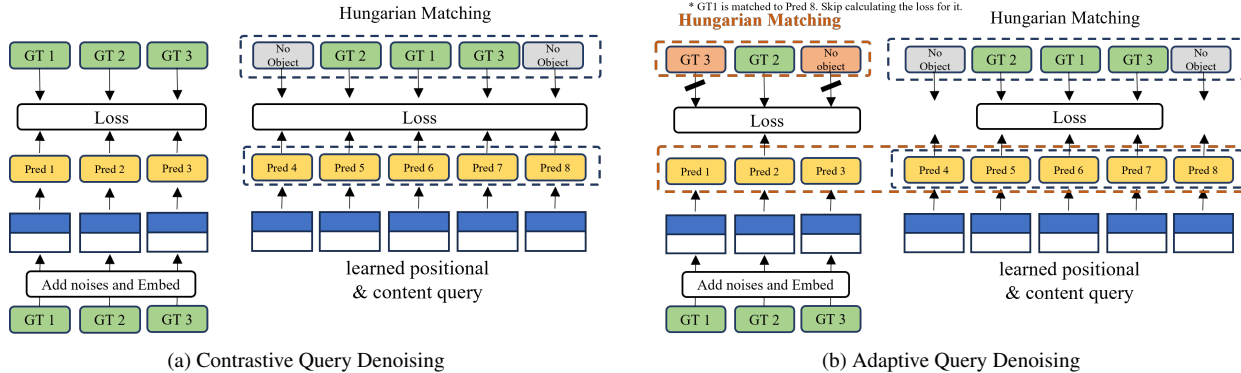


Figure 3. The comparison between contrastive query denoising and proposed adaptive query denoising.

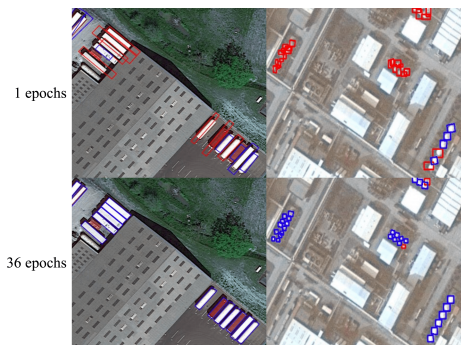


Figure 4. Visualization of adaptive query denoising. Adaptive query denoising reduces **unhelpful queries** as **predictions** become more accurate.

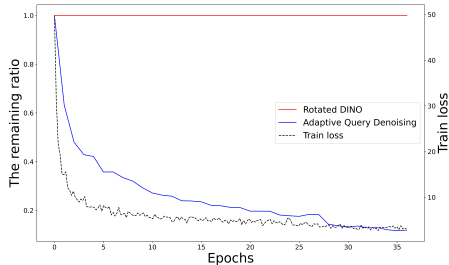


Figure 5. The ratio of positive noise queries to the denoising loss that changes during training.

$$\mathbf{p}^{\text{all}} = [\mathbf{p}^{\text{pos}}; \mathbf{p}] = [p_0^{\text{pos}}, p_1^{\text{pos}}, \dots, p_{M-1}^{\text{pos}}, p_0, p_1, \dots, p_{N-1}], \quad (6)$$

$$\hat{\sigma} = \underset{\sigma \in \mathfrak{S}}{\operatorname{argmin}} \sum_{i=0}^{M+N-1} \mathcal{L}_{\text{match}}(\hat{y}_i, \mathbf{p}_{\sigma_i}^{\text{all}}), \quad (7)$$

where  $\mathfrak{S}$  is the set of all permutations of size  $M + N - 1$  and  $\hat{y}_i$  is a padded version of ground truth objects.  $\mathcal{L}_{\text{match}}(\hat{y}_i, \mathbf{p}_{\sigma_i}^{\text{all}})$  represents a pair-wise matching cost between a ground truth  $\hat{y}_i$  and  $\mathbf{p}^{\text{all}}$  with index  $\sigma_i$ . This indicates that only positive queries whose matching index is

the same as the index where they were generated from the ground truth are used in the base training objective.

As illustrated in Figure 4 and Figure 5, the proposed adaptive query denoising effectively eliminates unhelpful noised queries as the predictions become more accurate through training. Building upon this method, we devise *improved adaptive query denoising* method. This enhancement involves adding a regression loss for the filtered positive queries to the original ground truth, which is formulated as:

$$\mathcal{L}_{\text{pos}}^*(p_i^{\text{pos}}, y_i) = \mathcal{L}_{\text{pos}}(p_i^{\text{pos}}, y_i) + \mathbb{1}_{\{\hat{\sigma}_i \neq i\}} \mathcal{L}_{\text{bbox}}(p_i^{\text{pos}}, y_i). \quad (8)$$

The rationale behind this modification is based on the idea that guiding the model to classify regions significantly far from the actual target as the target can lead to erroneous predictions, such as mistaking background areas for objects. To address this issue, we posit that maintaining a regression loss for the filtered positive queries could be still beneficial to the model. This strategy helps guide the model in refining its localization of predictions, especially those that are initially less accurate.

### 3. Experiments

#### 3.1. Experiment Setting

**Dataset.** We evaluate our proposed models on four datasets: DOTA-v1.0 [47]/v1.5/v2.0 [14], and DIOR-R [9] under single-scale training and testing setting. DOTA-v1.0/v1.5/v2.0 differ in the number of categories and the size of the training and test dataset. Unless otherwise specified, ablation studies are conducted on DOTA-v1.0. For all datasets, we use `train set`, `val set` for training and `test set` for evaluation. Evaluations on DOTA-v1.0/v1.5/v2.0 are conducted in the official DOTA evaluation server.

**Implementation Details.** The implementation details of our final model, RHINO, are described in Appendix 7. Unless explicitly stated otherwise, we adhere to the default hy-



Method	Backbone	PL	BD	BR	GTF	SV	LV	SH	TC	BC	ST	SBF	RA	HA	SP	HC	CC	AP	HL	AP <sub>50</sub>
R <sup>3</sup> Det w/ KLD [56]	R-50	-	-	-	-	-	-	-	-	-	-	-	-	-	-	-	-	-	-	50.90
Roi Trans. [13]	R-50	71.81	48.39	45.88	64.02	42.09	54.39	59.92	82.70	63.29	58.71	41.04	52.82	53.32	56.18	57.94	25.71	63.72	8.70	52.81
Oriented R-CNN [48]	R-50	77.95	50.29	46.73	65.24	42.61	54.56	60.02	79.08	61.69	59.42	42.26	56.89	51.11	56.16	59.33	25.81	60.67	9.17	53.28
DCFL [49]	R-50	78.30	53.03	44.24	60.17	48.56	55.42	58.66	78.29	60.89	65.93	43.54	55.82	53.33	60.00	54.76	30.90	74.01	15.60	55.08
DCFL [49]	ReR-101	79.49	55.97	50.15	61.59	49.00	55.33	59.31	81.18	66.52	60.06	52.87	56.71	57.83	58.13	60.35	35.66	78.65	13.03	57.66
Roi Trans. w/ [4]	ViT-G12×4 (MAE)	80.12	54.12	50.07	65.68	43.98	60.07	67.85	79.11	64.38	60.56	45.98	58.26	58.31	64.82	69.84	32.78	89.37	11.07	58.69
RHINO (Ours)	R-50	79.32	58.33	46.06	65.79	57.25	58.38	68.53	80.46	63.27	73.01	48.69	57.80	56.21	60.04	59.06	42.70	78.96	12.84	<b>59.26</b>
RHINO (Ours)	Swin-T	79.74	58.79	48.13	67.12	57.21	59.11	69.48	83.54	65.14	74.05	47.93	60.49	58.43	63.25	55.59	48.49	82.06	14.40	<b>60.72</b>

Table 2. Main results on DOTA-v2.0 test set under single-scale training and testing. **Red** and **blue**: top two performances.

Method	Backbone	PL	BD	BR	GTF	SV	LV	SH	TC	BC	ST	SBF	RA	HA	SP	HC	CC	AP	HL	AP <sub>50</sub>
EMO2-DETR [23]	R-50	71.81	75.36	45.09	58.70	48.19	73.26	80.28	90.70	73.05	76.53	39.36	65.31	56.96	69.29	47.11	15.64			61.67
Mask R-CNN [21]	R-50	76.84	73.51	49.90	57.80	51.31	71.34	79.75	90.46	74.21	66.07	46.21	70.61	63.07	64.46	57.81	9.42			62.67
HTC [6]	R-50	77.80	73.67	51.40	63.99	51.54	73.31	80.31	90.48	75.12	67.34	48.51	70.63	64.84	64.48	55.87	5.15			63.40
AO <sup>2</sup> -DETR [10]	R-50	79.55	78.14	42.41	61.23	55.34	74.50	79.57	90.64	74.76	77.58	53.56	66.91	58.56	73.11	69.64	24.71			66.26
ReDet [19]	ReR-50	79.20	82.81	51.92	71.41	52.38	75.73	80.92	90.83	75.81	68.64	49.29	72.03	73.36	70.55	63.33	11.53			66.86
DCFL [49]	R-50	-	-	-	-	56.72	-	80.87	-	-	75.65	-	-	-	-	-	-	-	-	67.37
DCFL [49]	ReR-101	-	-	-	-	52.38	-	86.60	-	-	76.55	-	-	-	-	-	-	-	-	70.24
RHINO (Ours)	R-50	77.96	83.22	55.30	72.14	65.07	78.95	89.22	90.78	80.90	83.48	61.58	74.17	77.21	71.99	60.16	29.26			<b>71.96</b>
RHINO (Ours)	Swin-T	79.96	85.16	56.96	74.50	64.14	81.91	89.42	90.60	83.93	82.89	59.93	74.84	77.23	75.18	64.91	33.76			<b>73.46</b>

Table 3. Main results on DOTA-v1.5 test set under single-scale training and testing. **Red** and **blue**: top two performances.

perparameters as outlined in DINO [62]. In our default configuration, the Hausdorff is computed using the four corner points of the bounding box coordinates.

### 3.2. Main Results

We compare our models with their counterparts that use an ImageNet pre-trained ResNet-50 backbone on DOTA-v2.0, DOTA-v1.5, DOTA-v1.0, and DIOR-R in order. Table 2 presents the results of our proposed model, RHINO, compared to state-of-the-art models in DOTA-v2.0, which is one of the largest remote sensing datasets. Our model with ResNet-50 backbone outperforms all other counterparts, even surpassing models with an advanced backbone such as ReResNet [19] or ViT-G12×4 (MAE)[16]. In addition, our model with Swin-Tiny establishes a new state-of-the-art with **60.72** AP<sub>50</sub>. Table 3 shows a comparison of our proposed RHINO with state-of-the-art models on the DOTA-v1.5 dataset. It also outperforms all other counterparts, with **73.46** AP<sub>50</sub>. We compare our proposed RHINO with state-of-the-art models on the DOTA-v1.0 dataset under single-scale training and testing in Table 4. RHINO consistently outperforms all other models.

For DIOR-R, Table 5 shows RHINO with ResNet-50 surpasses other models with ResNet-50, and the model with a heavier and domain-specific pre-trained backbone (ReR-101 and ViTAE-B + RVSA (MAE) [45]). Furthermore, using Swin-Tiny as a backbone leverages the performance to **72.67** AP<sub>50</sub>.

### 3.3. High-precision Evaluation of Rotated Object Detection

Zeng et al. [61] have underscored that AP<sub>50</sub> may not be the most appropriate metric for evaluating a model’s ability to accurately predict the orientation of objects, as it permits

large angle deviations. The authors argued that AP<sub>75</sub> is a more rigorous metric for assessing the performance in oriented object detection. Table 6 presents a comparison of our model with other models in terms of AP<sub>50</sub> and AP<sub>75</sub> on the DOTA-v1.0. Here, we also have conducted ablation studies to assess the impact of various IoU metrics, both in terms of matching cost and regression loss, on the performance of our model. Specifically, We compare our default IoU metric, the KLD loss [56], with the other alternatives like GWD [55], Rotated IoU (RIoU) [64], and GRIOU, the rotated variant of the generalized intersection over union [43]. The results indicate that our model excels not only in AP<sub>50</sub> but also in AP<sub>75</sub>, outperforming other models, including those specifically pre-trained for accurate rotated representation. Furthermore, our results indicate that using RIoU loss, including GRIOU, significantly enhances the performance in AP<sub>75</sub> compared to the models trained with metrics based on the 2-D Gaussian distribution.

### 3.4. Ablation Studies

Table 7 shows ablation experiments of the proposed module and other options.

**Ablation studies of proposed components.** Table 7a demonstrates the performance improvement by proposed components. Here, AQD and AQD\* represent adaptive query denoising and *improved adaptive query denoising*, outlined in Equation 5 and Equation 8, respectively. The baseline is our implementation of the rotated Deformable DETR. Applying the Hausdorff cost and the adaptive query denoising results in an increase in AP<sub>50</sub> to **78.05** and in AP<sub>75</sub> to **50.59**. Moreover, as mentioned in Section 2.5, when *improved adaptive query denoising* is applied, both AP<sub>50</sub> and AP<sub>75</sub> improve to **78.68** and **51.17**, respectively.

**Duplicate prediction comparison according to  $\mathcal{L}_{L1}$ .**

Method	Backbone	PL	BD	BR	GTF	SV	LV	SH	TC	BC	ST	SBF	RA	HA	SP	HC	AP <sub>50</sub>
EMO2-DETR [23]	R-50	88.08	77.91	43.17	62.91	74.01	75.09	79.21	90.88	81.50	84.04	51.92	59.44	64.74	71.81	58.96	70.91
EMO2-DETR [23]	Swin-T	89.03	79.59	48.71	60.23	77.34	76.42	84.53	90.77	84.80	85.68	48.86	67.55	66.32	71.54	53.49	72.32
ARS-DETR [61]	R-50	86.61	77.26	48.84	66.76	78.38	78.96	87.40	90.61	82.76	82.19	54.02	62.61	72.64	72.80	64.96	73.79
ARS-DETR [61]	Swin-T	87.78	78.58	52.58	67.69	80.19	84.32	88.19	90.68	85.92	84.76	55.18	66.89	74.57	79.09	60.35	75.79
RoI Trans. [13] (reported by [58])	R-50	89.02	81.71	53.84	71.65	79.00	77.76	87.85	90.90	87.04	85.70	61.73	64.55	75.06	71.71	62.38	75.99
ReDet [19]	ReR-50	88.79	82.64	53.97	74.00	78.13	84.06	88.04	90.89	87.78	85.75	61.76	60.39	75.96	68.07	63.59	76.25
Oriented RCNN [48]	R-50	89.46	82.12	54.78	70.86	78.93	83.00	88.20	90.90	87.50	84.68	63.97	67.69	74.94	68.84	52.28	75.87
Oriented RCNN [48]	R-101	88.86	83.48	55.27	76.92	74.27	82.10	87.52	90.90	85.56	85.33	65.51	66.82	74.36	70.15	57.28	76.28
R <sup>3</sup> Det-KLD [56]	R-50	88.90	84.17	55.80	69.35	78.72	84.08	87.00	89.75	84.32	85.73	64.74	61.80	76.62	78.49	70.89	77.36
AO <sup>2</sup> -DETR [10]	R-50	89.27	84.97	56.67	74.89	78.87	82.73	87.35	90.50	84.68	85.41	61.97	69.96	74.68	72.39	71.62	77.73
RoI Trans. w/ KFIOU [58]	Swin-T	88.9	83.77	53.98	77.63	78.83	84.22	88.15	90.91	87.21	86.14	67.79	65.73	75.80	73.68	63.30	77.74
RTMDet-R-m [38]	CSPNeXt-m	89.17	84.65	53.92	74.67	81.48	83.99	88.71	90.85	87.43	87.20	59.39	66.68	77.71	82.40	65.28	78.24
RTMDet-R-l [38]	CSPNeXt-l	89.43	84.21	55.20	75.06	80.81	84.53	88.97	90.90	87.38	87.25	63.09	67.87	78.09	80.78	69.13	78.85
Oriented R-CNN w/ [45]	ViTAE-B + RVSA(MAE)	89.38	84.26	59.39	73.19	79.99	85.36	88.08	90.87	88.50	86.53	58.93	72.24	77.31	79.59	71.24	<b>78.99</b>
RHINO (Ours)	R-50	88.28	85.19	55.89	72.75	80.23	83.14	89.07	90.88	87.12	86.89	65.37	71.68	77.75	81.24	64.71	78.68
RHINO (Ours)	Swin-T	88.18	84.77	58.54	77.73	81.13	85.58	89.18	90.86	86.96	86.38	65.49	71.29	78.17	82.80	64.26	<b>79.42</b>

Table 4. Main results on DOTA-v1.0 test set under single-scale training and testing. ReR-50 indicates ReResNet-50 [19]. **Red** and **blue**: top two performances.

Method	Backbone	AP <sub>50</sub>
Rotated RetinaNet [31]	R-50	57.55
Rotated Faster R-CNN [42]	R-50	59.54
RoI Trans. [13]	R-50	63.87
DCFL [49]	R-50	66.80
DCFL [49]	ReR-101	71.03
Oriented R-CNN w/ [45]	ViTAE-B + RVSA(MAE)	71.05
RHINO (Ours)	R-50	<b>71.79</b>
RHINO (Ours)	Swin-T	<b>72.67</b>

Table 5. Performance comparison on DIOR-R. **Red** and **blue**: top two performances.

Method	Backbone	# points	AP <sub>50</sub>	AP <sub>75</sub>
Oriented RCNN [48]	R-50	-	74.19	46.96
RoI Trans. [13]	R-50	-	74.05	46.54
RoI Trans. [13]	Swin-T	-	76.49	50.15
ReDet [19]	ReR-50	-	76.25	50.86
ARS-DETR [61]	R-50	-	73.79	49.01
ARS-DETR [61]	Swin-T	-	75.79	51.11
RHINO w/ KLD	R-50	32	<b>78.49</b>	51.84
RHINO w/ GWD	R-50	32	<b>77.87</b>	51.49
RHINO w/ RIoU	R-50	32	77.68	<b>53.51</b>
RHINO w/ GRIOU	R-50	32	77.24	<b>53.91</b>

Table 6. High-precision comparison on DOTA-v1.0. # points indicates the number of points for the Hausdorff distance. All results are reported by Zeng et al. [61].

We conduct ablation studies on the DOTA-v1.0 patch validation set for the L1 term,  $\mathcal{L}_{L1}$ , to evaluate alternative approaches that could address the duplicate predictions problem, as discussed in Section 2.3. Here, *None* means that we set  $\lambda_{L1}$ , the weight for  $\mathcal{L}_{L1}$ , to 0 and XYWH-L1 represents the L1 distance using  $\{b_x, b_y, b_w, b_h\}$ . Table 7b summarizes the results of these ablation experiments. The results indicate that replacing the L1 distance with the Hausdorff distance for the matching cost yields notable performance improvements and effectively reduces duplicate predictions. While other metrics can be utilized to minimize duplicate predictions, the Hausdorff distance shows the best performance both with and without NMS.

#### Effects of the number of points for the Hausdorff. We

check the impact of the number of points for the Hausdorff distance. The results are shown in Table 7c. We can observe that 4 points get the best performance of 78.68 in AP<sub>50</sub>. In AP<sub>75</sub> for high-precision, 32 points achieve the best performance of 51.84.

**Analysis of the impact of aspect ratios.** To evaluate the effectiveness of the Hausdorff distance in addressing the issue of duplicate predictions, we conducted a class-wise performance comparison using the DOTA-v1.0 patch validation set. The results, detailed in Table 8, reveal that using the Hausdorff distance significantly improves performance for square-like objects, such as baseball-diamond, storage-tank, and roundabout.

## 4. Related Work

### 4.1. Query-based Object Detection

Contrary to the conventional object detectors, Carion et al. [3] introduced a query-based object detector called DETR (Detection Transformer) that eliminates the need for hand-designed components such as anchor design and NMS. Despite achieving comparable results to Faster-RCNN [42], DETR’s training is hindered by slow convergence. Consequently, numerous studies have attempted to accelerate the training process of DETR. They include addressing the inefficiency of cross-attention in Transformer decoders [11, 22, 28, 67], designing dynamic or encoder-only DETR models [7, 32, 44], improving decoder queries [5, 33, 35, 63] and advanced label assignment strategies [2, 8, 24, 29, 34].

**Query Denoising Strategies** The main part of this study is closely related to the query denoising methodology, specifically focusing on DN-DETR [27] and DINO [62] as two representative works in this area. DN-DETR [27] introduces a novel denoising training method to accelerate DETR training and address its slow convergence issue. The authors attribute the slow convergence to the instability of

DINO	Hausdorff	AQD	AQD*	AP <sub>50</sub>	AP <sub>75</sub>
				70.48	40.78
✓				74.56	49.63
✓	✓			76.14	50.33
✓	✓	✓		78.05	50.59
✓			✓	76.63	50.97
✓	✓		✓	<b>78.68</b>	<b>51.17</b>

(a) Ablation study of proposed components.

Cost	Loss	Angle Def.	AP <sub>50</sub>	w/ NMS
L1	L1	Long Edge	67.99	+1.34
L1	L1	OpenCV	69.26	+0.58
XYWH L1	XYWH L1	Long Edge	69.88	+0.04
XYWH L1	L1	Long Edge	69.84	+0.03
None	None	Long Edge	68.30	+0.10
None	L1	Long Edge	70.18	-0.26
Hausdorff	L1	Long Edge	70.81	-0.09

(b) Duplicate prediction comparison on patch-based validation according to  $\mathcal{L}_{L1}$ .

# points	AQD*	AP <sub>50</sub>	AP <sub>75</sub>
4	✓	78.68	51.17
8	✓	78.12	51.02
32	✓	78.49	51.84

(c) Ablation on the number of points for the Hausdorff distance.

Table 7. Ablation studies of model architecture on DOTA-v1.0.

class	Aspect Ratio	L1	Hausdorff
plane	0.7982	89.0	89.8
baseball-diamond	<b>0.9239</b>	<b>67.1</b>	<b>71.5</b>
bridge	0.4350	48.6	50.9
ground-track-field	0.5044	66.3	66.8
small-vehicle	0.4736	69.2	69.1
large-vehicle	0.2746	84.5	83.7
ship	0.3535	87.7	88.4
tennis-court	0.4828	90.6	90.5
basketball-court	0.5748	60.0	56.7
storage-tank	<b>0.9365</b>	<b>63.3</b>	<b>73.1</b>
soccer-ball-field	0.6109	56.2	58.2
roundabout	<b>0.9224</b>	<b>52.3</b>	<b>60.8</b>
harbor	0.4018	75.8	76.5
swimming-pool	0.6087	53.7	54.9
helicopter	0.7146	55.5	71.4
AP <sub>50</sub>	0.4705	68.0	70.81

Table 8. Class-wise performance and its average aspect ratios on the patch validation set.

bipartite graph matching in the early training stages. By feeding ground-truth bounding boxes with noise into the Transformer decoder and training the model to reconstruct the original boxes, DN-DETR effectively reduces the bipartite graph matching difficulty and achieves faster convergence. DINO [62] builds upon the training method and further enhances performance and efficiency by using a contrastive approach for query denoising. Both of these models have demonstrated significant improvements in the training and performance of DETR-like methods. In contrast to existing methodologies, our adaptive query denoising approach concentrates on the adaptive reduction of redundant positive queries during the later training phase. This strategy is particularly effective when the model has reached a stage of proficiency where its predictive accuracy surpasses that of the noise-influenced ground truths.

## 4.2. Oriented Object Detection

In the literature, oriented object detection methods can generally be categorized into three classes: (1) improved neural network architectures, (2) enforcing equivalence and invariance of representation, and (3) devising appropriate angle/box representations and loss functions. Methods in the first category [26, 40, 49, 57] aim to enhance neural network architectures to better handle rotated objects. The second category [18, 19, 48] focuses on developing layers or structures that provide equivalence and invariance of representa-

tion for rotated object detection, which is crucial for effective angle regression and classification. The third category [41, 48, 49, 51, 52, 55, 56, 59, 60] concentrates on proposing appropriate angle or oriented bounding box representations and loss functions to address the challenges arising from the circularity of angles.

Query-based detectors have recently been extended to tackle rotated object detection tasks in a number of studies [10, 39, 61, 65]. AO2-DETR [10] introduces an oriented proposal generation mechanism and an adaptive oriented proposal refinement module, while O2-DETR [39] adopts an efficient encoder for the transformer by replacing the attention mechanism with depthwise separable convolution. ARS-DETR [61] proposes an Aspect Ratio-aware Circle Smooth Label and a rotated deformable attention module, and D2Q-DETR [65] focuses on decoupling query features and dynamic query design. EMO2-DETR [23] proposes efficient matching to pose relative redundancy problem of object queries. Although these methodologies have shown that query-based detectors are useful for oriented object detection, the performance of these methods on high-precision oriented object detection tasks still has room for improvement.

## 5. Conclusions

This study presents a strong DETR that outperforms the traditional oriented object detectors. Our comprehensive analysis demonstrates the square-like problem, caused by the L1 cost, which impedes the non-duplicate predictions of DETR. To this end, we introduce the Hausdorff distance to replace the L1 cost in Hungarian Matching. Furthermore, we tackled the limitations of the static denoising approach in rotated DETR training. Our adaptive query denoising technique, which leverages Hungarian matching, effectively filters out irrelevant noised queries, thereby enhancing the training process and the model’s overall performance. The state-of-the-art performance of our RHINO on benchmarks demonstrates its significant potential for rotated object detection. This study contributes a strong DINO-based baseline for oriented object detection and underscores the potential of query-based object detectors, setting the stage for future research in this domain.



## References

- [1] Hedy Attouch, Roberto Lucchetti, and Roger J-B Wets. The topology of the  $\rho$ -hausdorff distance. *Annali di Matematica pura ed applicata*, 160(1):303–320, 1991. [4](#)
- [2] Zhi Cai, Songtao Liu, Guodong Wang, Zheng Ge, Xiangyu Zhang, and Di Huang. Align-detr: Improving detr with simple iou-aware bce loss. *arXiv preprint arXiv:2304.07527*, 2023. [2](#), [7](#)
- [3] Nicolas Carion, Francisco Massa, Gabriel Synnaeve, Nicolas Usunier, Alexander Kirillov, and Sergey Zagoruyko. End-to-end object detection with transformers. In *Computer Vision–ECCV 2020: 16th European Conference, Glasgow, UK, August 23–28, 2020, Proceedings, Part I 16*, pages 213–229. Springer, 2020. [2](#), [3](#), [7](#)
- [4] Keumgang Cha, Junghoon Seo, and Taekyung Lee. A billion-scale foundation model for remote sensing images. *arXiv preprint arXiv:2304.05215*, 2023. [6](#)
- [5] Fangyi Chen, Han Zhang, Kai Hu, Yu-kai Huang, Chenchen Zhu, and Marios Savvides. Enhanced training of query-based object detection via selective query recollection. In *Proceedings of the IEEE/CVF international conference on computer vision*, 2022. [7](#)
- [6] Kai Chen, Jiangmiao Pang, Jiaqi Wang, Yu Xiong, Xiaoxiao Li, Shuyang Sun, Wansen Feng, Ziwei Liu, Jianping Shi, Wanli Ouyang, Chen Change Loy, and Dahua Lin. Hybrid task cascade for instance segmentation. In *Proceedings of the IEEE/CVF conference on computer vision and pattern recognition*, pages 4974–4983, 2019. [6](#)
- [7] Peixian Chen, Mengdan Zhang, Yunhang Shen, Kekai Sheng, Yuting Gao, Xing Sun, Ke Li, and Chunhua Shen. Efficient decoder-free object detection with transformers. In *Computer Vision–ECCV 2022: 17th European Conference, Tel Aviv, Israel, October 23–27, 2022, Proceedings, Part X*, pages 70–86. Springer, 2022. [7](#)
- [8] Qiang Chen, Xiaokang Chen, Gang Zeng, and Jingdong Wang. Group detr: Fast training convergence with decoupled one-to-many label assignment. *arXiv preprint arXiv:2207.13085*, 2022. [7](#)
- [9] Gong Cheng, Jiabao Wang, Ke Li, Xingxing Xie, Chunbo Lang, Yanqing Yao, and Junwei Han. Anchor-free oriented proposal generator for object detection. *IEEE Transactions on Geoscience and Remote Sensing*, 60:1–11, 2022. [5](#)
- [10] Linhui Dai, Hong Liu, Hao Tang, Zhiwei Wu, and Pinhao Song. Ao2-detr: Arbitrary-oriented object detection transformer. *IEEE Transactions on Circuits and Systems for Video Technology*, 2022. [2](#), [6](#), [7](#), [8](#)
- [11] Xiyang Dai, Yinpeng Chen, Jianwei Yang, Pengchuan Zhang, Lu Yuan, and Lei Zhang. Dynamic detr: End-to-end object detection with dynamic attention. In *Proceedings of the IEEE/CVF International Conference on Computer Vision*, pages 2988–2997, 2021. [7](#)
- [12] Jia Deng, Wei Dong, Richard Socher, Li-Jia Li, Kai Li, and Li Fei-Fei. Imagenet: A large-scale hierarchical image database. In *2009 IEEE conference on computer vision and pattern recognition*, pages 248–255. Ieee, 2009. [13](#)
- [13] Jian Ding, Nan Xue, Yang Long, Gui-Song Xia, and Qikai Lu. Learning roi transformer for oriented object detection in aerial images. In *2019 IEEE/CVF Conference on Computer Vision and Pattern Recognition (CVPR)*, pages 2844–2853, 2019. [1](#), [2](#), [6](#), [7](#), [13](#)
- [14] Jian Ding, Nan Xue, Guisong Xia, Xiang Bai, Wen Yang, Micheal Ying Yang, Serge J. Belongie, Jiebo Luo, Mihai Datcu, Marcello Pelillo, and L. Zhang. Object detection in aerial images: A large-scale benchmark and challenges. *IEEE transactions on pattern analysis and machine intelligence*, 44(11):7778–7796, 2021. [5](#)
- [15] Jian Ding, Nan Xue, Guisong Xia, Xiang Bai, Wen Yang, Micheal Ying Yang, Serge J. Belongie, Jiebo Luo, Mihai Datcu, Marcello Pelillo, and L. Zhang. Object detection in aerial images: A large-scale benchmark and challenges. *IEEE transactions on pattern analysis and machine intelligence*, 44(11):7778–7796, 2021. [1](#)
- [16] Alexey Dosovitskiy, Lucas Beyer, Alexander Kolesnikov, Dirk Weissenborn, Xiaohua Zhai, Thomas Unterthiner, Mostafa Dehghani, Matthias Minderer, Georg Heigold, Sylvain Gelly, et al. An image is worth 16x16 words: Transformers for image recognition at scale. *arXiv preprint arXiv:2010.11929*, 2020. [6](#)
- [17] Zonghao Guo, Chang Liu, Xiaosong Zhang, Jianbin Jiao, Xiangyang Ji, and Qixiang Ye. Beyond bounding-box: Convex-hull feature adaptation for oriented and densely packed object detection. In *Proceedings of the IEEE/CVF Conference on Computer Vision and Pattern Recognition*, pages 8792–8801, 2021. [2](#)
- [18] Jiaming Han, Jian Ding, Jie Li, and Gui-Song Xia. Align deep features for oriented object detection. *IEEE Transactions on Geoscience and Remote Sensing*, 60:1–11, 2021. [1](#), [8](#), [13](#)
- [19] Jiaming Han, Jian Ding, Nan Xue, and Gui-Song Xia. Redet: A rotation-equivariant detector for aerial object detection. In *Proceedings of the IEEE/CVF Conference on Computer Vision and Pattern Recognition*, pages 2786–2795, 2021. [1](#), [6](#), [7](#), [8](#), [13](#)
- [20] Kaiping He, Xiangyu Zhang, Shaoqing Ren, and Jian Sun. Deep residual learning for image recognition. In *Proceedings of the IEEE conference on computer vision and pattern recognition*, pages 770–778, 2016. [13](#)
- [21] Kaiping He, Georgia Gkioxari, Piotr Dollár, and Ross Girshick. Mask r-cnn. In *Proceedings of the IEEE international conference on computer vision*, pages 2961–2969, 2017. [6](#)
- [22] Liqiang He and Sinisa Todorovic. Destr: Object detection with split transformer. In *Proceedings of the IEEE/CVF conference on computer vision and pattern recognition*, pages 9377–9386, 2022. [7](#)
- [23] Zibo Hu, Kun Gao, Xiaodan Zhang, Junwei Wang, Hong Wang, Zhijia Yang, Chenrui Li, and Wei Li. Emo2-detr: Efficient-matching oriented object detection with transformers. *IEEE Transactions on Geoscience and Remote Sensing*, 2023. [6](#), [7](#), [8](#)
- [24] Ding Jia, Yuhui Yuan, Haodi He, Xiaopei Wu, Haojun Yu, Weihong Lin, Lei Sun, Chao Zhang, and Han Hu. Detsr with hybrid matching. In *Proceedings of the IEEE/CVF international conference on computer vision*, 2023. [7](#)
- [25] Diederik P Kingma and Jimmy Ba. Adam: A method for

- stochastic optimization. *arXiv preprint arXiv:1412.6980*, 2014. **13**
- [26] Jamyoungh Koo, Junghoon Seo, Seunghyun Jeon, Jeongyeol Choe, and Taegyun Jeon. Rbox-cnn: Rotated bounding box based cnn for ship detection in remote sensing image. In *Proceedings of the 26th ACM SIGSPATIAL International Conference on Advances in Geographic Information Systems*, page 420–423, New York, NY, USA, 2018. Association for Computing Machinery. **1, 8**
- [27] Feng Li, Hao Zhang, Shilong Liu, Jian Guo, Lionel M Ni, and Lei Zhang. Dn-detr: Accelerate detr training by introducing query denoising. In *Proceedings of the IEEE/CVF Conference on Computer Vision and Pattern Recognition*, pages 13619–13627, 2022. **3, 4, 7, 12, 13**
- [28] Feng Li, Ailing Zeng, Shilong Liu, Hao Zhang, Hongyang Li, Lei Zhang, and Lionel M Ni. Lite detr: An interleaved multi-scale encoder for efficient detr. In *Proceedings of the IEEE conference on computer vision and pattern recognition*, 2023. **7**
- [29] Shuai Li, Minghan Li, Ruihuang Li, Chenhang He, and Lei Zhang. One-to-few label assignment for end-to-end dense detection. In *Proceedings of the IEEE conference on computer vision and pattern recognition*, 2013. **7**
- [30] Tsung-Yi Lin, Michael Maire, Serge Belongie, James Hays, Pietro Perona, Deva Ramanan, Piotr Dollár, and C Lawrence Zitnick. Microsoft coco: Common objects in context. In *Computer Vision—ECCV 2014: 13th European Conference, Zurich, Switzerland, September 6–12, 2014, Proceedings, Part V 13*, pages 740–755. Springer, 2014. **2**
- [31] Tsung-Yi Lin, Priya Goyal, Ross Girshick, Kaiming He, and Piotr Dollár. Focal loss for dense object detection. In *Proceedings of the IEEE international conference on computer vision*, pages 2980–2988, 2017. **3, 7**
- [32] Fanfan Liu, Haoran Wei, Wenzhe Zhao, Guozhen Li, Jingquan Peng, and Zihao Li. Wb-detr: transformer-based detector without backbone. In *Proceedings of the IEEE/CVF International Conference on Computer Vision*, pages 2979–2987, 2021. **7**
- [33] Shilong Liu, Feng Li, Hao Zhang, Xiao Yang, Xianbiao Qi, Hang Su, Jun Zhu, and Lei Zhang. DAB-DETR: Dynamic anchor boxes are better queries for DETR. In *International Conference on Learning Representations*, 2022. **2, 3, 7, 12**
- [34] Siyi Liu, Tianhe Ren, Jia-Yu Chen, Zhaoyang Zeng, Hao Zhang, Feng Li, Hongyang Li, Jun Huang, Hang Su, Jun-Juan Zhu, and Lei Zhang. Detection transformer with stable matching. *arXiv preprint arXiv:2304.04742*, 2023. **7**
- [35] Yang Liu, Yao Zhang, Yixin Wang, Yang Zhang, Jiang Tian, Zhongchao Shi, Jianping Fan, and Zhiqiang He. Sap-detr: Bridging the gap between salient points and queries-based transformer detector for fast model convergency. In *Proceedings of the IEEE/CVF international conference on computer vision*, 2023. **7**
- [36] Ze Liu, Yutong Lin, Yue Cao, Han Hu, Yixuan Wei, Zheng Zhang, Stephen Lin, and Baining Guo. Swin transformer: Hierarchical vision transformer using shifted windows. In *Proceedings of the IEEE/CVF international conference on computer vision*, pages 10012–10022, 2021. **13**
- [37] Ilya Loshchilov and Frank Hutter. Decoupled weight decay regularization. *arXiv preprint arXiv:1711.05101*, 2017. **13**
- [38] Chengqi Lyu, Wenwei Zhang, Haian Huang, Yue Zhou, Yudong Wang, Yanyi Liu, Shilong Zhang, and Kai Chen. RtmDET: An empirical study of designing real-time object detectors. *arXiv preprint arXiv:2212.07784*, 2022. **7, 13**
- [39] Teli Ma, Mingyuan Mao, Honghui Zheng, Peng Gao, Xiaodi Wang, Shumin Han, Errui Ding, Baochang Zhang, and David Doermann. Oriented object detection with transformer. *arXiv preprint arXiv:2106.03146*, 2021. **2, 8**
- [40] Qi Ming, Zhiqiang Zhou, Lingjuan Miao, Hongwei Zhang, and Linhao Li. Dynamic anchor learning for arbitrary-oriented object detection. *Proceedings of the AAAI Conference on Artificial Intelligence*, 35(3):2355–2363, 2021. **1, 8**
- [41] Wen Qian, Xue Yang, Silong Peng, Junchi Yan, and Yue Guo. Learning modulated loss for rotated object detection. *Proceedings of the AAAI Conference on Artificial Intelligence*, 35(3):2458–2466, 2021. **1, 8**
- [42] Shaoqing Ren, Kaiming He, Ross Girshick, and Jian Sun. Faster r-cnn: Towards real-time object detection with region proposal networks. *Advances in neural information processing systems*, 28, 2015. **7**
- [43] Hamid Rezaatofghi, Nathan Tsoi, JunYoung Gwak, Amir Sadeghian, Ian Reid, and Silvio Savarese. Generalized intersection over union: A metric and a loss for bounding box regression. In *Proceedings of the IEEE/CVF conference on computer vision and pattern recognition*, pages 658–666, 2019. **3, 6**
- [44] Zhiqing Sun, Shengcao Cao, Yiming Yang, and Kris M Kitani. Rethinking transformer-based set prediction for object detection. In *Proceedings of the IEEE/CVF international conference on computer vision*, pages 3611–3620, 2021. **7**
- [45] Di Wang, Qiming Zhang, Yufei Xu, Jing Zhang, Bo Du, Dacheng Tao, and Liangpei Zhang. Advancing plain vision transformer towards remote sensing foundation model. *IEEE Transactions on Geoscience and Remote Sensing*, 2022. **6, 7**
- [46] Wenhai Wang, Jifeng Dai, Zhe Chen, Zhenhang Huang, Zhiqi Li, Xizhou Zhu, Xiaowei Hu, Tong Lu, Lewei Lu, Hongsheng Li, et al. InternImage: Exploring large-scale vision foundation models with deformable convolutions. *arXiv preprint arXiv:2211.05778*, 2022. **2**
- [47] Gui-Song Xia, Xiang Bai, Jian Ding, Zhen Zhu, Serge Belongie, Jiebo Luo, Mihai Datcu, Marcello Pelillo, and Liangpei Zhang. Dota: A large-scale dataset for object detection in aerial images. In *Proceedings of the IEEE conference on computer vision and pattern recognition*, pages 3974–3983, 2018. **1, 3, 5**
- [48] Xingxing Xie, Gong Cheng, Jiabao Wang, Xiwen Yao, and Junwei Han. Oriented r-cnn for object detection. In *Proceedings of the IEEE/CVF International Conference on Computer Vision*, pages 3520–3529, 2021. **1, 6, 7, 8, 13**
- [49] Chang Xu, Jian Ding, Jinwang Wang, Wen Yang, Huai Yu, Lei Yu, and Gui-Song Xia. Dynamic coarse-to-fine learning for oriented tiny object detection. In *Proceedings of the IEEE/CVF Conference on Computer Vision and Pattern Recognition*, 2023. **1, 6, 7, 8**

- [50] Jianwei Yang, Chunyuan Li, Xiyang Dai, and Jianfeng Gao. Focal modulation networks. *Advances in Neural Information Processing Systems*, 35:4203–4217, 2022. [2](#)
- [51] Xue Yang and Junchi Yan. Arbitrary-oriented object detection with circular smooth label. In *Computer Vision – ECCV 2020*, pages 677–694, Cham, 2020. Springer International Publishing. [1](#), [8](#)
- [52] Xue Yang, Liping Hou, Yue Zhou, Wentao Wang, and Junchi Yan. Dense label encoding for boundary discontinuity free rotation detection. In *2021 IEEE/CVF Conference on Computer Vision and Pattern Recognition (CVPR)*, pages 15814–15824, 2021. [8](#)
- [53] Xue Yang, Liping Hou, Yue Zhou, Wentao Wang, and Junchi Yan. Dense label encoding for boundary discontinuity free rotation detection. In *Proceedings of the IEEE/CVF conference on computer vision and pattern recognition*, pages 15819–15829, 2021. [1](#), [4](#)
- [54] Xue Yang, Junchi Yan, Ziming Feng, and Tao He. R3det: Refined single-stage detector with feature refinement for rotating object. In *Proceedings of the AAAI conference on artificial intelligence*, pages 3163–3171, 2021. [13](#)
- [55] Xue Yang, Junchi Yan, Qi Ming, Wentao Wang, Xiaopeng Zhang, and Qi Tian. Rethinking rotated object detection with gaussian wasserstein distance loss. In *Proceedings of the 38th International Conference on Machine Learning*, pages 11830–11841. PMLR, 2021. [2](#), [4](#), [6](#), [8](#), [12](#)
- [56] Xue Yang, Xiaojiang Yang, Jirui Yang, Qi Ming, Wentao Wang, Qi Tian, and Junchi Yan. Learning high-precision bounding box for rotated object detection via kullback-leibler divergence. In *Advances in Neural Information Processing Systems*, pages 18381–18394. Curran Associates, Inc., 2021. [3](#), [4](#), [6](#), [7](#), [8](#), [12](#)
- [57] X. Yang, J. Yan, W. Liao, X. Yang, J. Tang, and T. He. Scrdet++: Detecting small, cluttered and rotated objects via instance-level feature denoising and rotation loss smoothing. *IEEE Transactions on Pattern Analysis and Machine Intelligence*, 45(02):2384–2399, 2023. [2](#), [8](#)
- [58] Xue Yang, Yue Zhou, Gefan Zhang, Jitui Yang, Wentao Wang, Junchi Yan, Xiaopeng Zhang, and Qi Tian. The KFIou loss for rotated object detection. In *The Eleventh International Conference on Learning Representations*, 2023. [7](#), [12](#)
- [59] Xue Yang, Yue Zhou, Gefan Zhang, Jirui Yang, Wentao Wang, Junchi Yan, XIAOPENG ZHANG, and Qi Tian. The KFIou loss for rotated object detection. In *The Eleventh International Conference on Learning Representations*, 2023. [2](#), [8](#)
- [60] Yi Yu and Feipeng Da. Phase-shifting coder: Predicting accurate orientation in oriented object detection. In *2023 IEEE/CVF Conference on Computer Vision and Pattern Recognition (CVPR)*, 2023. [2](#), [8](#)
- [61] Ying Zeng, Xue Yang, Qingyun Li, Yushi Chen, and Junchi Yan. Ars-detr: Aspect ratio sensitive oriented object detection with transformer. *arXiv preprint arXiv:2303.04989*, 2023. [2](#), [6](#), [7](#), [8](#), [12](#)
- [62] Hao Zhang, Feng Li, Shilong Liu, Lei Zhang, Hang Su, Jun Zhu, Lionel Ni, and Heung-Yeung Shum. DINO: DETR with improved denoising anchor boxes for end-to-end object detection. In *The Eleventh International Conference on Learning Representations*, 2023. [2](#), [3](#), [6](#), [7](#), [8](#), [12](#), [13](#)
- [63] Shilong Zhang, Wang xinjiang, Jiaqi Wang, Jiangmiao Pang, Chengqi Lyu, Wenwei Zhang, Ping Luo, and Kai Chen. Dense distinct query for end-to-end object detection. In *Proceedings of the IEEE conference on computer vision and pattern recognition*, 2023. [7](#)
- [64] Dingfu Zhou, Jin Fang, Xibin Song, Chenye Guan, Junbo Yin, Yuchao Dai, and Ruigang Yang. Iou loss for 2d/3d object detection. In *2019 international conference on 3D vision (3DV)*, pages 85–94. IEEE, 2019. [6](#)
- [65] Qiang Zhou, Chaohui Yu, Zhibin Wang, and Fan Wang. D2q-detr: Decoupling and dynamic queries for oriented object detection with transformers. In *IEEE International Conference on Acoustics, Speech and Signal Processing (ICASSP)*, 2023. [2](#), [8](#)
- [66] Yue Zhou, Xue Yang, Gefan Zhang, Jiabao Wang, Yanyi Liu, Liping Hou, Xue Jiang, Xingzhao Liu, Junchi Yan, Chengqi Lyu, Wenwei Zhang, and Kai Chen. Mmrotate: A rotated object detection benchmark using pytorch. In *Proceedings of the 30th ACM International Conference on Multimedia*, pages 7331–7334, 2022. [13](#)
- [67] Xizhou Zhu, Weijie Su, Lewei Lu, Bin Li, Xiaogang Wang, and Jifeng Dai. Deformable {detr}: Deformable transformers for end-to-end object detection. In *International Conference on Learning Representations*, 2021. [2](#), [3](#), [7](#), [12](#)
- [68] Zhuofan Zong, Guanglu Song, and Yu Liu. Detsr with collaborative hybrid assignments training. *arXiv preprint arXiv:2211.12860*, 2022. [2](#)



## 6. Implementation Details of Our Baseline

In this section, we elaborate on the challenges that specifically occur when introducing rotated DETRs.

### Angle Prediction by Simple Extended Box Regressor.

In the DETRs, the coordinates of objects are handled as normalized ranges  $[0, 1]$  (relative to the image size) in the training stage. The normalized predicted coordinates from the sigmoid function are recovered to the original range by multiplying the width and height of the input image. One straightforward way to enable DETRs to predict the angle of an object is to extend the output of the regression head to  $\mathbf{b} \in [0, 1]^5$ , where  $\mathbf{b} = \{b_x, b_y, b_w, b_h, b_{rad}\}$  denotes the normalized center coordinates, box width and height, and the angle in radians, respectively. In this case, the angle also should be treated as normalized values like center coordinates and width and height. We adopt Long Edge Definition ( $\theta \in [0, \pi)$ ) to treat angle values in the range  $[0, 1]$  and normalize the angles by  $\pi$  so that the values fit in the range  $[0, 1]$ . By treating angles the same way as other coordinate values, rather than introducing a dedicated angle prediction branch, the model can easily incorporate other developed components related to coordinates, such as iterative bounding box refinement, handling queries as anchor boxes, and proposing queries from the feature map of the encoder.

**Replacement of GIoU Loss.** The standard costs and losses used in DETRs are Focal loss, L1 loss, and GIoU loss. However, calculating overlaps between two rotated objects is commonly known to be indifferentiable [55, 56, 58]. Therefore, we need to consider alternative options to replace GIoU loss for rotated objects. Two representative substitutes for representing the error between predictions and ground truth for rotated objects are Gaussian Wasserstein Distance (GWD) [55] and Kullback-Leibler Divergence (KLD) [56]. The center distance term in GWD and KLD also works as the penalty term for non-overlapping bounding boxes, similar to GIoU loss. We adopt KLD as our baseline to replace the GIoU cost and loss since previous work has shown that KLD outperforms GWD in oriented object detection. Additionally, we set the weight for the IoU term from 2 to 5 based on the comparison experiment, which is shown in Table 9. This weight is applied to all our experiments except the experiments conducted on the patch validation set.

**Rotated Deformable Attention.** In order to address the slow convergence and computational/memory complexity associated with the multi-head attention module in the original DETR, Zhu et al. [67] proposed a deformable attention

$\mathcal{L}_{L1}$ Cost	$\mathcal{L}_{L1}$ Loss	$\lambda_{iou}$	AP <sub>50</sub>	w NMS
None	None	2	68.30	+0.10
None	None	5	70.18	-0.05
Hausdorff	L1	2	70.81	-0.09
Hausdorff	L1	5	70.94	+0.16

Table 9. Performance comparison on the patch validation set.

module. This module takes an input feature map and either 2D reference points  $\mathbf{p}_2 = (p_x, p_y)$  or 4D reference boxes  $\mathbf{p}_4 = (p_x, p_y, p_w, p_h)$ , where  $(p_x, p_y)$  represents a series of center coordinates and  $(p_w, p_h)$  represents a series of widths and heights for the reference boxes, to determine the sampling location. The sampling locations for 2D reference points are obtained by adding the predicted sampling offsets to the given reference points. In the case of 4D reference boxes, the predicted sampling offsets are first added to the center coordinates of reference boxes. Then, the resulting values are multiplied by half of the widths and heights of the reference boxes to determine the final 2D coordinates for the sampling locations. These 4D reference boxes are used here to boost the performance through the iterative refinement and the query proposal from the encoder.

As Zeng et al. [61] pointed out, using  $\{b_x, b_y, b_w, b_h\}$  as reference boxes from 5D reference boxes by dropping  $b_{rad}$  leads to feature misalignment, especially in deformable attention modules. We apply a similar way to Zeng et al. [61] to rotate the center coordinates from the reference boxes. The predicted normalized angles are recovered by multiplying the normalized factor  $\pi$ , and the next steps follow the case of 4D reference boxes as described previously. In contrast to the approach proposed by Zeng et al. [61], we update 5D reference boxes including angles during the iterative refinement step. To update the 5D reference boxes, we apply the inverse sigmoid function to the reference points and add the resulting values to the logit of the regression head in logit space. We then normalize the updated values using the sigmoid function, which maps them to the range of  $[0, 1]$ . The same update logic is also applied to the predicted regression in the head part.

**Extension to DINO.** By straightforwardly extending the regression head with 5D rotated boxes, the model is able to naturally adopt the developed mechanisms such as queries as dynamic anchor boxes proposed by successive works [27, 33, 62]. Here, we just brief some implementation details to note. The two-stage scheme introduced by Deformable-DETR [67], requires **generating grid proposals from the encoded features**, and predicting query proposals by running the regression head to the encoded features. In our implementation, We use zero-angle grids to generate grid proposals from the encoded features and run the regression head on the flattened feature vectors. This allows

Model	Epochs	IR	Two-Stage	5D RP	5D Head	AP <sub>50</sub>
Deformable DETR	50	-	-	-	-	68.50
Deformable DETR	50	✓	-	-	-	68.54
Deformable DETR	50	✓	✓	-	-	70.48
DINO	12	✓	✓	-	-	71.36
DINO	12	✓	✓	✓	-	72.76
DINO	12	✓	✓	✓	✓	76.10

Table 10. Ablation studies on our baseline. ‘5D RP’ refers to the updating angles of 5D reference points in Decoder layers. ‘5D Head’ refers to the updating angles of predictions using reference points in the head module. No checkmark in ‘5D RP’ or ‘5D Head’ columns indicates that only the coordinates  $\{b_x, b_y, b_w, b_h\}$  of the reference points or predictions are updated.

the regression output to be added directly to the proposals. For **denoising training** [27, 62], we add noises only to  $\{b_x, b_y, b_w, b_h\}$  for simplicity. We exclude the angle for the decoder positional queries which are related to **mixed query selection** in DINO [62]. Finally, we experiment with models using 900 queries and set the maximum number of predictions to 500 to handle densely packed objects in remote sensing images.

**Updating Angles in Logit Space.** Table 10 presents some results from our ablation studies on the updating angles. We first started by not updating the angle of reference points or predictions due to the simplicity of this approach and the challenges in interpreting the implications of summing angles in logit space. For example, adding the angles 100 degrees and 100 degrees equals 200 degrees, resulting in 20 degrees in the long edge definition. However, we only expect that it will be near 180 degree when they are summed in logit space and recovered to the original degree. However, our experiment shows that treating the angle similar to other coordinates can lead to improved performance.

## 7. Implementation Details of RHINO

We implement our models on MMRotate [66] v1.0.0rc1. Most of our experiments are conducted on 2 NVIDIA V100 GPUs with a total batch size of 8. Two backbones: ResNet-50 [20] and Swin-Tiny [36] are used in our experiments, both of which are pre-trained on ImageNet-1k [12]. We use the AdamW [25, 37] optimizer with an initial learning rate of  $1 \times 10^{-4}$ . We use a step decay learning rate schedule where the learning rate is multiplied by 0.1 at the 11th epoch during the 12 epoch training and multiplied by 0.1 again at the 27th and 33rd epochs during the 36 epoch training. For DOTA-v1.0/v1.5/v2.0, we crop each image in the data sets to  $1024 \times 1024$  pixels with a 200-pixel overlap. The input size of experiments on DIOR-R is set to  $800 \times 800$ . We use only horizontal, vertical, and diagonal flips without additional augmentations.

Method	Dataset	AP <sub>50</sub>	Hmean <sub>50</sub>
DINO	SKU110K-R	87.22	-
RHINO		88.30	-
DINO	MSRA-TD500	-	0.5862
RHINO		-	0.6173
DINO	ICDAR2015	-	0.5685
RHINO		-	0.5819

Table 11. Performance comparison on Rotated Object Datasets.

Method	Backbone	mAP <sub>07</sub>	mAP <sub>12</sub>
RoI Trans. [13]	R-101	86.20	-
R <sup>3</sup> Det [54]	R-101	89.26	96.01
S <sup>2</sup> ANet [18]	R-101	90.17	95.01
Oriented R-CNN [48]	R-50	90.40	96.50
ReDet [19]	ReR-50	90.46	97.63
RTMDet-R-tiny [38]	CSPNeXt-tiny	<b>90.60</b>	97.10
DINO [62] (Our implementation)	R-50	90.26	97.37
RHINO (Ours)	R-50	90.30	<b>97.86</b>

Table 12. Performance comparison on HRSC2016.

## 8. Experiments on Other Rotated Object Datasets

We extend the evaluation of our model, RHINO, by comparing it with the DINO baseline across various other rotated object detection datasets. Specifically, we focus on two scene text detection datasets, MSRA-TD500 and ICDAR2015, as well as the retail object dataset SKU110K-R. For the MSRA-TD500 dataset, we trained both RHINO and DINO models for 50 epochs. For the SKU110K-R and ICDAR2015 datasets, the training duration was set to 36 epochs. As detailed in Table 11, RHINO consistently outperforms the DINO baseline, demonstrating its robustness and effectiveness even though these datasets generally include non-square objects.

Table 12 presents a comparison between our model and state-of-the-art models on the HRSC2016, which is a widely used aerial ship dataset for oriented object detection. While our model, RHINO, exhibits marginally lower performance than the state-of-the-art models in terms of mAP<sub>07</sub>, it is noteworthy that RHINO surpasses all other models in mAP<sub>12</sub>.

## 9. Visualization

Figure 6 presents a qualitative comparison of our models and other models. Notably, the RoI Transformer demonstrates lower precision in predicting object angles compared to our model and ARS-DETR.

Figure 7 and Figure 8 provide further comparisons between the baseline and our model. Overall, RHINO exhibits relatively consistent non-duplicate predictions compared to the baseline, especially in square-like objects, as

shown in Figure 8. However, it is important to note that RHINO occasionally produces duplicate predictions on the MSRA-TD500 dataset. We assume this is due to the small amount of training dataset for MSRA-TD500.

## 10. Limitation

One significant limitation of employing the Hausdorff distance is its memory usage, which scales linearly with the number of queries and ground truths. This becomes particularly challenging when combined with the denoising training strategy, which generates a multiple of the number of original ground truths. Consequently, applying the Hausdorff distance cost with denoising training becomes significantly limited by the memory requirements in scenes with a large number of ground truths, requiring higher GPU memory in multi-scale training settings.



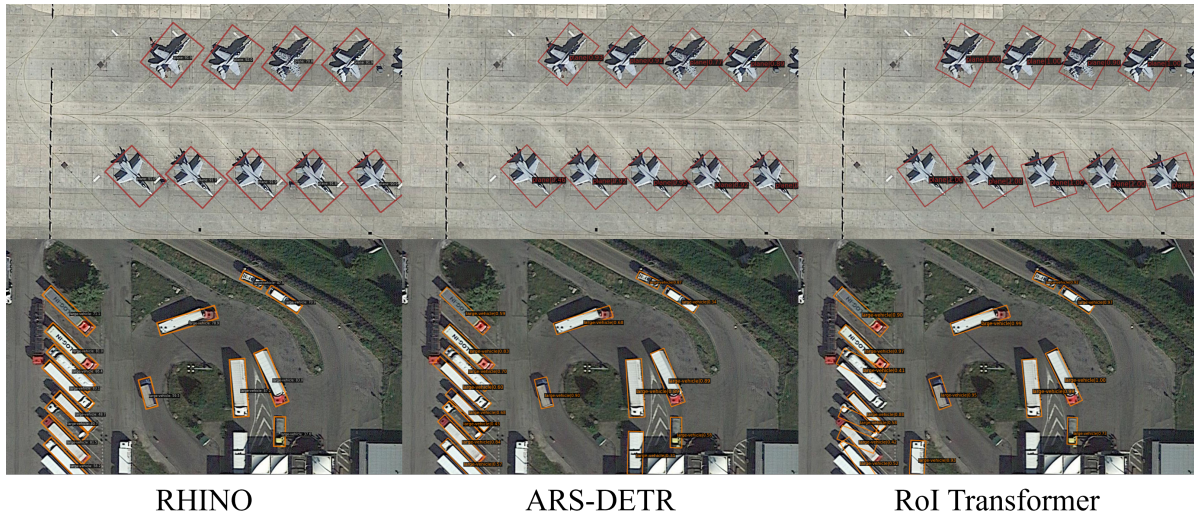


Figure 6. Qualitative comparison between our model and other models on the DOTA-v1.0 dataset.



Figure 7. Qualitative comparison between the baseline and our model on the MSRA-TD500 dataset.



DINO

RHINO

Figure 8. Qualitative comparison between the baseline and our model on the SKU110K-R dataset.